Understanding hydrogen electrocatalysis by probing the hydrogen-bond network of water at the electrified Pt/solution interface

Qiang Sun[1], Nicholas J. Oliveira[2], Soonho Kwon[3], Sergiy Tyukhtenko[4], Jason J. Guo[1,5], Nathalie Myrthil[1], Steven A. Lopez[1], Ian Kendrick[1], Sanjeev Mukerjee[1], Lu Ma[6], Steven N. Ehrlich[6], Jingkun Li[7]*, William A. Goddard III[3*], Yushan Yan[2*], and Qingying Jia[1&*]

[1]Department of Chemistry and Chemical Biology, Northeastern University; Boston, Massachusetts, 02115, United States.

[2]Center for Catalytic Science and Technology, Department of Chemical and Biomolecular Engineering, University of Delaware; Newark, Delaware, 19716, United States.

[3]Liquid Sunlight Alliance (LiSA) and Materials and Process Simulation Center (MSC), California Institute of Technology, Pasadena, California 91125, United States.

[4]Center for Drug Discovery and Departments of Pharmaceutical Sciences and Chemistry and Chemical Biology, Northeastern University; Boston, Massachusetts, 02115, United States.

[5]Barnett Institute for Chemical & Biological Analysis, Northeastern University; Boston, Massachusetts, 02115, United States.

[6]National Synchrotron Light Source II, Brookhaven National Laboratory; Upton, New York, 11973, United States.

[7]School of Chemistry and Molecular Engineering, East China University of Science and Technology; Shanghai, 200237, China.

[&]Current address, Plug Power *Inc*, Concord, Massachusetts, 01742, United States

*Correspondence authors. Emails: lijingkun1987@gmail.com (J. L.); wagoddard3@gmail.com (W. G.); yanys@udel.edu (Y. Y.); qjia@iit.edu (Q. J.)

ORCID: WAG:0000-0003-0097-5716

Abstract. A grand challenge in electrochemistry is to understand and promote electrochemical processes by exploring and exploiting the interface. Herein, we promoted the hydrogen evolution and oxidation reactions (HER/HOR) of platinum (Pt) in base by introducing N-methylimidazoles into the Pt-water interface. *In situ* spectroscopic characterization of the interface together with Quantum Mechanics computations showed that this promotion is caused by the N-methylimidazoles facilitating diffusion of hydroxides across the interface by holding the second layer water close to Pt surfaces. We accordingly propose that the HER/HOR kinetics of Pt in acid and base is governed by diffusion of protons and hydroxides, respectively, through the hydrogen-bond network of interfacial water by the Grotthuss mechanism, which accounts for the pH-dependent HER/HOR kinetics of platinum, a long-standing puzzle. Moreover, we demonstrated a 40% performance improvement of an anion exchange membrane electrolyzer by adding 1,2-dimethylimidazole into the alkaline solution fed into its platinum cathode.

The pH has profound influences on the kinetics of electrochemical processes such as hydrogen electrocatalysis. The activity of the hydrogen evolution and oxidation reactions (HER/HOR) of several transition metals including platinum (Pt) progressively decreases as the pH increases[1-3]. The reason(s) behind this phenomenon has remained unclear despite decades of studies. One primary strategy adopted in these studies is to mix Pt with another metal such as Ni or Ru to improve its HER/HOR activity in alkaline, followed by identifying the promoting roles of Ni/Ru[4-10]. However, different groups proposed different promoting roles of Ni/Ru and suggested different causes for the sluggish HER/HOR of Pt in alkaline. Some groups stated that the Ru/Ni improves the HER/HOR of Pt by weakening the binding energy between Pt and hydrogen (E_{PtH}) via strain and/or electronic effects, and ascribed the sluggish HER/HOR of Pt in alkaline to the overly strong E_{PtH}[8-11]. Other groups proposed that Ru/Ni promotes water dissociation/formation owing to its high oxophilicity and attributed the sluggish HER/HOR of Pt in base to the high energy barriers of water dissociation/formation[4,6,7]. The Koper and Feliu groups showed that the Ni deposited on Pt surfaces negatively shifts the potential of zero free charge (pzfc), which eases the flip of interfacial water, and in turn promotes the HER/HOR of Pt[12-14]. They accordingly attributed the pH-dependence of the HER/HOR activity of Pt to the pH-dependent pzfc[15,16]. We recently identified the promoting role of Ru as facilitating interfacial water shuffling of the HER/HOR intermediates[17]. Because of the ambiguity over the promoting roles of Ni/Ru, this strategy has not led to a conclusive explanation of the sluggish HER/HOR kinetics of Pt in alkaline. Finding other promoters with definitive promoting roles may give definitive answers to this open question and provide alternative routes to promote the HER/HOR of Pt in alkaline.

The Snyder group[18] recently found that adding caffeine into alkaline solution substantially improved the HER/HOR activity of Pt, but the mechanism for this improvement was unclear. This work inspired us to seek other organic compounds that promote HER/HOR of Pt in alkaline and then to identify their promoting roles to understand the HER/HOR kinetics of Pt. By studying a set of N-methylimidazoles via a combination of rotating disk electrode (RDE), nuclear magnetic resonance (NMR), and Quantum Mechanics computations, we found that the more negatively charged pyridinic nitrogen (N_3) of N-methylimidazole forms a stronger hydrogen-bond (H-bond) with interfacial H_2O and gives greater improvements of the HER/HOR rate of Pt. *In situ* attenuated total reflectance surface-enhanced infrared reflection absorption spectroscopy (ATR-SEIRAS) coupled with surface-enhanced Raman and ab initio molecular dynamics (AIMD) showed that 1,2-dimethylimidazole forms a strong $N_3\cdots H_2O$ bond with interfacial water. These findings enabled us to identify the promoting role of N-methylimidazoles in facilitating the Volmer step of Pt in alkaline.

N-methylimidazoles promoting the HER/HOR of Pt. We first verified that adding 10^{-5} M caffeine into 0.1 M KOH electrolyte markedly improved the HER/HOR activity of Pt/C (TKK, 47.7 wt%) (Fig. 1a) in a RDE as originally reported by Snyder and co-workers[18]. We then tested 10^{-5} M 1,3-dimethyluracil and 1-methylimidazole (Me-N_1), the left and right parts of caffeine, respectively, to determine which part(s) of caffeine contribute to the improvement. The 1,3-dimethyluracil did not promote the HER/HOR of Pt (Fig. 1b), whereas 1-methylimidazole did (Fig. 1c). Following this observation, we added a set of N-methylimidazoles with different numbers of methyl groups (-CH_3) located at different positions of the imidazole ring (Fig. 1d-i) into 0.1 M KOH to promote the HER/HOR of Pt/C, which renders delicate tailoring of the molecular structure of the probes. These compounds are accordingly labelled by the locations of

methyl groups hereafter (a list of the notions given in Supplementary Table 1). We quantified their improvements of the HER/HOR specific exchange current densities (i_0) of Pt/C by fitting the kinetic currents to the Butler–Volmer equation (Methods). The electrochemical surface area (ECSA) was derived from the hydrogen underpotential deposition (H_{upd}) charge of the cyclic voltammetry (*CV*) of Pt/C in 0.1 M KOH within the potential range of 0.05-0.45 V (versus reversible hydrogen electrode (RHE)). The average i_0 of Pt/C in these cases is 0.64±0.02 $mA \cdot cm_{Pt}^{-2}$, comparable to that (0.57±0.07 $mA \cdot cm_{Pt}^{-2}$) of Pt/C reported previously[19] under similar conditions. Although the H_{upd} charge of Pt/C was significantly suppressed by the N-methylimidazoles (Supplementary Fig. 2), likely via the steric effect, the HOR limiting current density remained unchanged for all cases. Moreover, the HER/HOR polarization curves overlapped with or without adding 10^{-5} M imidazole or 1,3-dimethyluracil (Supplementary Fig. 3). These phenomena indicate that these N-methylimidazoles do not block the Pt sites for the HER/HOR as spectators. We therefore used the H_{upd} charge of Pt/C obtained in the 0.1 M KOH electrolyte prior to addition of N-methylimidazoles as the ECSA of the Pt/C in 0.1 M KOH with N-methylimidazoles. Higher concentrations of 10^{-4} M and 10^{-3} M were found to give similar improvement as 10^{-5} M (Supplementary Fig. 4).

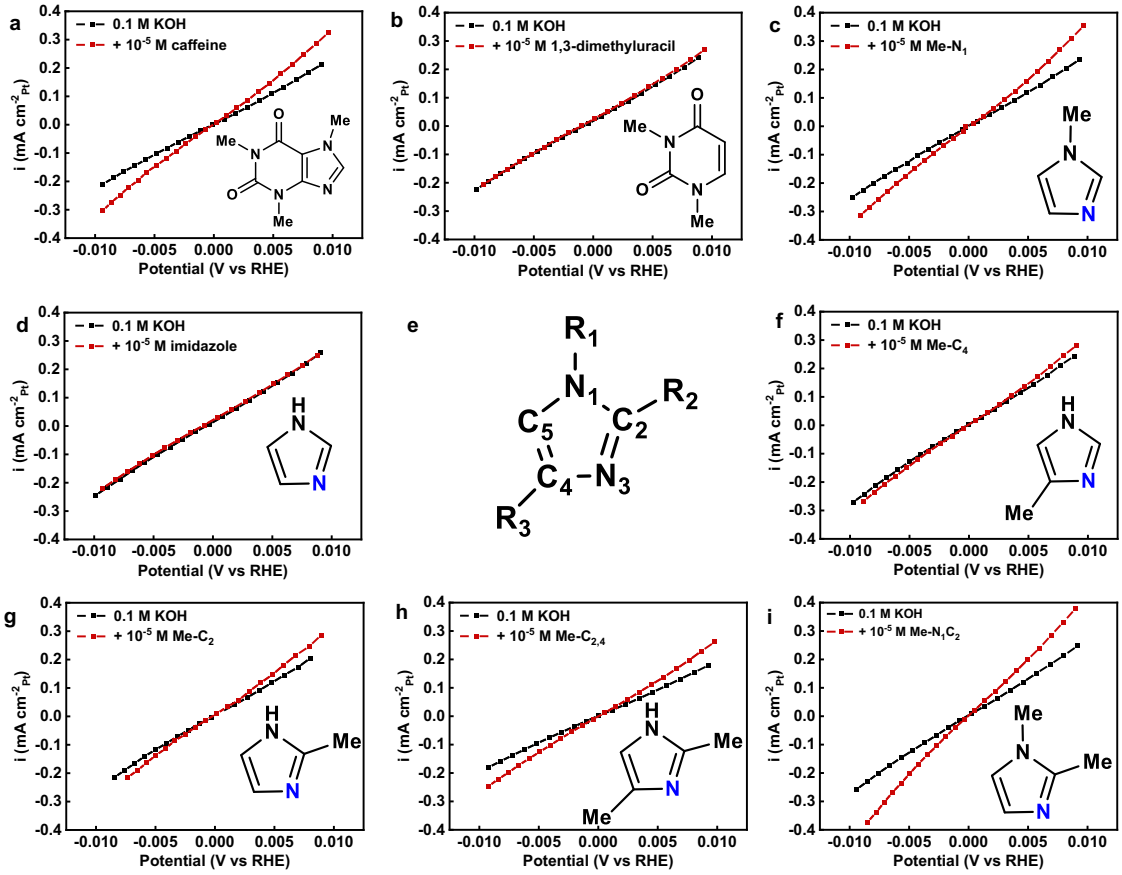

Fig. 1. Structurally dependent promotion effects of organic compounds on the HOR/HER of Pt. The *iR*-corrected HOR/HER low-overpotential kinetic current density of Pt/C (8 $\mu g_{Pt} \cdot cm^{-2}$) with or without 10^{-5} M (**a**) caffeine, (**b**) 1,3-dimethyluracil, (**d**) imidazole and (**c, f-i**) N-methylimidazoles in H_2-saturated 0.1 M KOH with a rotation rate of 2,500 rpm and a scan rate of 20 $mV \cdot s^{-1}$, room temperature. The structure of the corresponding compound is given in the inset. (**e**) illustrates the atomic numbering of the imidazole ring, and the $R_{1,2,3}$ represents possible location(s) for methyl group(s) in N-methylimidazoles. Full polarization curves are given in Supplementary Fig. 1.

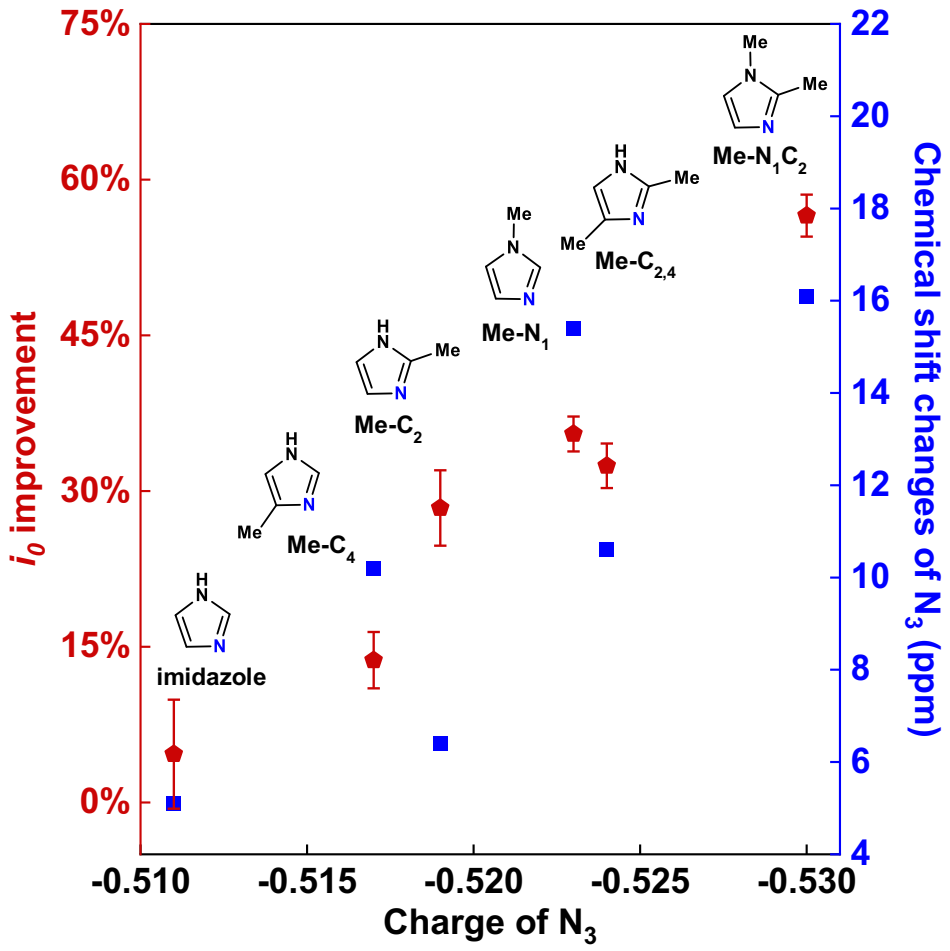

Fig. 2: N-methylimidazoles promote the HOR/HER of Pt through the $N_3\cdots H_2O$ bonding. The i_0 improvements (red dots, left y-axis) and the $^{14}N_3/^{15}N_3$ chemical shift changes (blue squares, right y-axis) of N-methylimidazoles between two different medias as a function of the charge of their N_3(s). The charges of the N_3 were determined by density functional theory (DFT), with the rapid averaging of the N_1 and N_3 charge via proton exchange[20] taken under consideration for imidazole, Me-C_2, Me-C_4, and Me-$C_{2,4}$ (Supplementary Note 1). The molecular structures of N-methylimidazoles are present with the N_3 in blue. Error bars represent the standard deviations from at least three independent electrochemical measurements. The $^{14}N_3/^{15}N_3$ chemical shift changes were obtained by subtracting the resonance peak position in 10% CD_2Cl_2+ 90% CH_2Cl_2 from that in 0.1 M KOH with 10% D_2O+ 90% H_2O (NMR spectra were given in Supplementary Fig. 5).

In general, the N-methylimidazoles with more -CH_3(s) give higher i_0 improvements (Fig. 2; Supplementary Table 1). No significant improvement was observed for imidazole that contains no -CH_3 (5±5%). As the number of -CH_3 increases, the i_0 improvement generally increases until reaching 57±2% for Me-N_1C_2 that contains two -CH_3(s). The position of -CH_3

also affects the improvement. The improvement of Me-N_1 (36±2%) with the -CH_3 bonded with N_1 is higher than those of Me-C_4 (14±3%) and Me-C_2 (28±4%). Similarly, the improvement of Me-N_1C_2 (57±2%) is higher than that of Me-$C_{2,4}$ (33±2%). By contrast, 1,3-dimethyluracil with the two -CH_3(s) bonded with N_1 and N_3 does not improve the i_0 of Pt/C (Fig. 1b), which suggests that -CH_3 alone does not promote the HER/HOR of Pt/C. Therefore, a wide range of i_0 improvements were achieved by varying the position and/or number of -CH_3 in the N-methylimidazoles.

N-methylimidazoles interacting with interfacial water. To identify the roles of -CH_3, we used DFT calculations to determine the partial charges of these N-methylimidazoles. We found that the i_0 improvement of these N-methylimidazoles increases monotonously with the negative charge of N_3 (Fig. 2), and the negative charge of N_3 is affected by the number and position of -CH_3 (Supplementary Table 2), a well-known electron-donating group. These results suggest that the -CH_3(s) affect the N-methylimidazoles-induced HER/HOR activity improvement of Pt through tuning the charge of N_3.

To elucidate the catalytic role of N_3, we conducted ^{14}N and ^{15}N NMR experiments on these N-methylimidazoles in 0.1 M KOH as well as in CH_2Cl_2 solution as a baseline because the N atoms in N-methylimidazoles have minimal interactions with CH_2Cl_2 (Ref[20]). When transferring from 0.1 M KOH to CH_2Cl_2 solution, the $^{14}N_3$ chemical shifts of Me-N_1 and Me-N_1C_2 exhibit a downfield shift of 15.4 and 16.1 ppm, respectively (details given in Supplementary Note 2). A comparable shift (15 ppm) was previously reported[20] by transferring Me-N_1 from 0.1 M KOH to CH_2Cl_2 and ascribed to the change of the bonding from $N_3\cdots H_2O$ to N_3. This change verifies the interaction between the lone-pair electrons of the N_3 and the H of the ($N_3\cdots H_2O$ bond), which has been widely observed in N-methylimidazole solvent[21]. Combining

the DFT, NMR with RDE results leads to the trend that Me-N_1C_2 exhibits a more negative N_3, stronger $N_3\cdots H_2O$ bond, and higher i_0 improvement than Me-N_1 (Fig. 2). The same trend is also observed between imidazole and Me-C_2 and between Me-C_4 and Me-$C_{2,4}$ (Fig. 2; Supplementary Table 1-3), with the only difference in each couple being an additional -CH_3 bonded with C_2. This trend indicates that the -CH_3(s) in the N-methylimidazoles tune the negative charge of N_3 and in turn the $N_3\cdots H_2O$ bond strength, thereby modulating the i_0 improvement. We infer from these results that the N-methylimidazoles promote the HER/HOR of Pt in 0.1 M KOH by the $N_3\cdots H_2O$ bonding.

In situ ATR-SEIRAS was then conducted to probe the effects of N-methylimidazoles on the interfacial water structure near Pt surfaces during the HER/HOR. Spectra were collected during potential steps in an H_2-saturated 0.1 M KOH solution with and without 10^{-5} M Me-N_1C_2. For both cases, the spectra collected at 0.5 V (double-layer region) were used as a baseline for subtraction. The characteristic features of interfacial water, two ν(OH) bands at ~3,500 and ~3,000 cm^{-1} (Fig. 3a) and a δ(HOH) band at ~1,610 cm^{-1} (Supplementary Fig. 6)[22-24], were observed in the spectra collected in 0.1 M KOH free of Me-N_1C_2 within the H_{upd} potential region. It has been established that water monomers possess ν(OH) bands around 3,700 cm^{-1}, and the H-bond among water molecules red-shifts and broadens the ν(OH) bands substantially for hydrogen donors but modestly for hydrogen acceptors[22,23]. Therefore, the broad band around 3,000 cm^{-1} is characteristic of the strongly hydrogen-bonded water structure composed of hydrogen donors close to the Pt surface; whereas the sharp band around 3,500 cm^{-1} arises from the weakly hydrogen-bonding water structure made of hydrogen acceptors[22]. Consistent with previous studies[22,24], the intensity of the ν(OH) band around 3,000 cm^{-1} progressively decreases as the potential reduces from 0.5 V to 0 V, accompanied by a slight growth of the ν(OH) band

between 3,300-3,500 cm^{-1}, and both bands blue-shift (Fig. 3a). These spectral changes have been ascribed to the potential-dependent reorientation of the H-up water (↑H_2O, proton donor) towards H-down water (↓H_2O, proton acceptor)[22,23]. This potential-dependent reorientation of interfacial water has also been observed by *in situ* Raman[25] and *in situ* X-ray diffraction[26], and rationalized by computations that Pt surfaces become more negatively charged with reducing potential (vs. RHE) and thus favor bonding with ↓H_2O over ↑H_2O[27]. However, the general trends of the *ν*(OH) bands are dramatically altered upon addition of 10^{-5} M Me-N_1C_2 into 0.1 M KOH. The 3,000 cm^{-1} band undergoes neither a decrease in intensity nor a blue-shift with potential (Fig. 3b), indicative of Me-N_1C_2 retaining the strong H-bond interfacial water near the Pt surface.

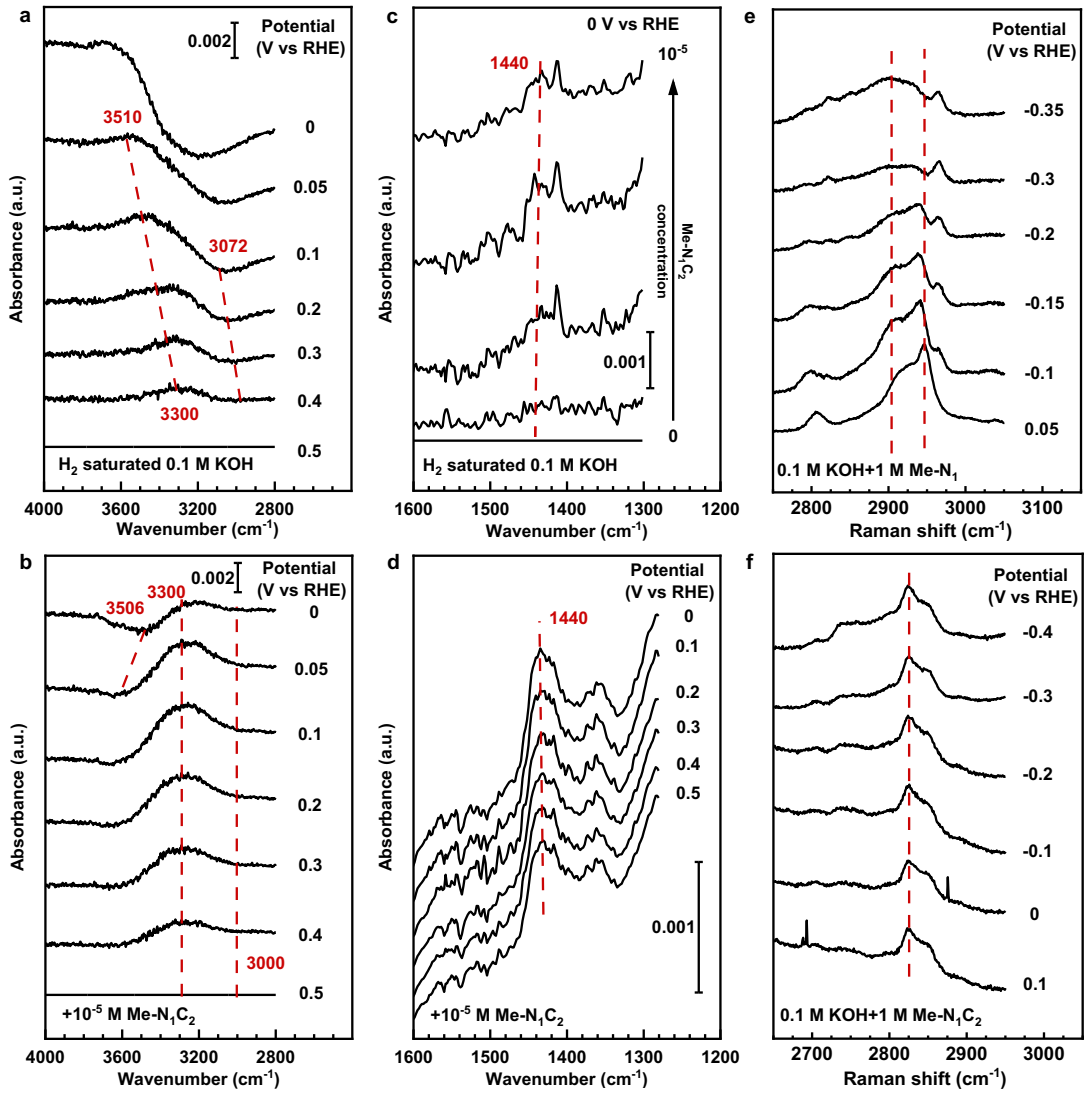

Fig. 3: ***In situ*** **probe of interfacial water and N-dimethylimidazoles**. The *in situ* ATR-SEIRAS spectra of interfacial water on a Pt film collected in 0.1 M KOH (**a**) without and (**b**) with 10^{-5} M Me-N_1C_2. (**c**) The *in situ* ATR-SEIRAS spectra of Me-N_1C_2 collected in 0.1 M KOH at 0 V with increasing concentration. (**d**) The *in situ* ATR-SEIRAS spectra of Me-N_1C_2 with a concentration of 10^{-5} M in 0.1 M KOH at various potentials. The *in situ* Raman spectra were collected in 0.1 M KOH with 1 M (**e**) Me-N_1 and (**f**) Me-N_1C_2 on an Ag electrode.

In situ ATR-SEIRAS also provided information of the binding configuration of the interfacial Me-N_1C_2. The peak at 1,440 cm^{-1}, which was identified as the C-H bending mode of the -CH_3 (Ref[28]), gradually grows upon the addition of Me-N_1C_2 into 0.1 M KOH when holding at 0 V (Fig. 3c), which is clearly reflected by the subtractive spectra (Supplementary Fig. 7). The

lack of a shift of this peak with changing potential (Fig. 3d) indicates the lack of stark effects of the -CH_3(s) and thus the lack of chemical bonding with the Pt surface[29]. This is further confirmed by X-ray absorption spectroscopy (XAS) from the Pt perspective. The XAS spectrum at the Pt L_3-edge remains unchanged upon adding 10^{-5} M Me-N_1C_2 onto the Pt XAS electrode despite the suppressed H_{upd} peaks (Supplementary Fig. 8), which suggests that the bonding between Me-N_1C_2 and Pt is not sufficiently strong or abundant to be detectable by the XAS, given that specific adsorption of H[30] and CO[31,32] on Pt/C change the Pt XAS spectrum markedly.

In situ Raman was implemented to probe the orientation of N-methylimidazoles near the silver (Ag) electrode in 0.1 M KOH, given that the feasibility of this method was demonstrated previously thanks to the enhancement effect of Ag on Raman signals[33]. The *in situ* Raman spectra of Me-N_1 exhibit two sets of dynamic peaks within 2,800-3,200 cm^{-1} in the potential range of -0.35 to -0.05 V (Supplementary Fig. 9a), matching well with those of Me-N_1 previously reported in 0.1 M KCl[33]. The growth and broadening of the $\nu(CH_3)$ bands between 2,850-2,950 cm^{-1} with reducing potential observed here (Fig. 3e) were previously reported[33] and ascribed to the potential dependent reorientation of Me-N_1. Specifically, the Me-N_1 interacts with the positively charged surface through the N_3 lone pair electrons at high potentials, while the -CH_3 points away from the surface, making the ring plane nearly normal to the surface. At low potentials the positive -CH_3 prefers to interact with the negatively charged surface via field-induced dipole interactions, rendering the ring largely parallel to the surface[33,34]. By contrast, the $\nu(CH_3)$ bands of Me-N_1C_2 are largely preserved within the potential range of -0.4 to -0.1 V (Fig. 3f). The same phenomenon was previously observed on Me-C_2 and explained as -CH_3 bonded with the C_2 next to N_3, so it remains close to the surface even when the positively charged surface interacts with N_3 and inhibits (Ref[33]). The divergent Raman results between Me-N_1 and

Me-N_1C_2 indicates that the -CH_3 bonded with the C_2 upholds the parallel configuration of the imidazole ring, which implicates a beneficial spatial effect of the -CH_3, in addition to modulating the charge of N_3. The spatial effect of -CH_3 found on the Ag surface shall be applicable to Pt surfaces despite possibly different ring-reorientation potentials given that our *in situ* ATR-SEIRAS showed the -CH_3 not forming chemical bonding with the Pt surfaces, which is further confirmed by AIMD as shown next.

N-methylimidazoles promoting the HER/HOR of Pt by facilitating hydroxide diffusion. To further examine the roles of Me-N_1C_2, we conducted AIMD simulations on the Pt(100)-water interface with and without Me-N_1C_2 in the explicit solvent (details given in Supplementary Note 3). Following our previous work using a hybrid scheme that combined implicit and explicit solvation,[35] we chose a net electron charge of 0 e^- and 3 e^- as the surface charge of Pt to represent the 0 V vs RHE in the acidic and alkaline working environment, respectively. The Pt(100)-water interface was first constructed without Me-N_1C_2 as a baseline. In the alkaline condition, all the water molecules in the first layer (closest to the surface) have the H-down orientation ($\downarrow H_2O^{1st}$) (Fig. 4a), owing to the interaction between the negatively charged surface and the dipole of O-H bonds. This is further manifested by the O distribution of the $\downarrow H_2O^{1st}$ along the axis perpendicular to the surface that gives an average distance of 3.14 Å (Fig. 4b). The $\downarrow H_2O^{1st}$ molecules (H-bond acceptors) form H-bonds with the $\downarrow H_2O^{2nd}$ molecules (H-bond donors), thereby constructing the interfacial H-bond network (Fig. 4a).

We then introduced Me-N_1C_2 into the Pt(100)-water interface with three binding configurations (Supplementary Fig. 10). Among them, the imidazole-ring binding in parallel to the surface (Fig. 4c) with the Pt-C and Pt-N bond distances within a narrow range of 2.1±0.1 Å and the non-chemical Pt-CH_3 bonds ≥ 2.9 Å (Supplementary Table 4) is the most energetically

favorable configuration, in agreement with our *in situ* ATR-SEIRAS and Raman results (Supplementary Note 3). In this configuration, the $\downarrow H_2O^{2nd}$ is an H-bond donor to both the $\uparrow H_2O^{1st}$ (Fig. 4c) and the N_3 of Me-N_1C_2, the latter in line with our NMR results.

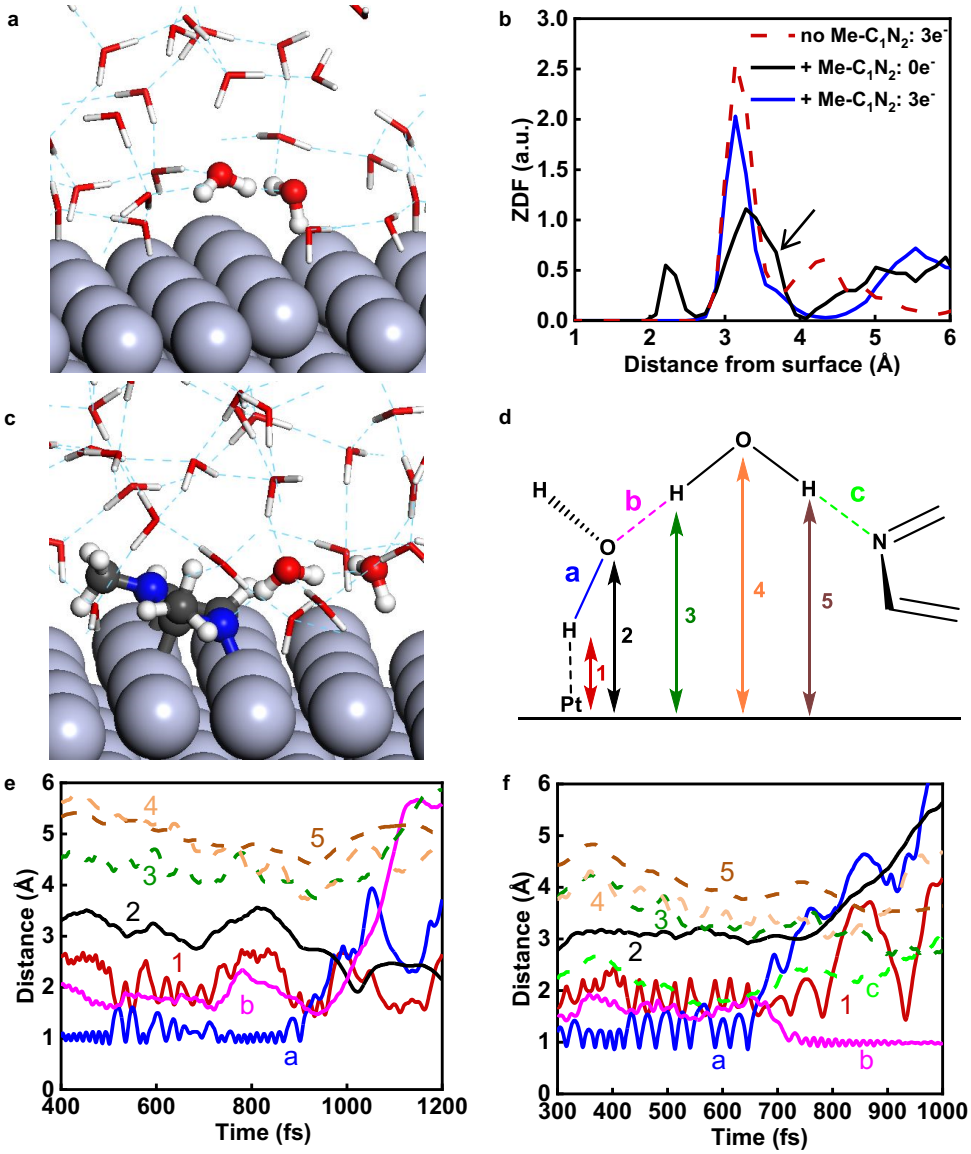

Fig. 4: The Vomer step at the H_2O/Pt(100) interface with/without Me-N_1C_2. (**a**) Atomic configuration of an equilibrated H_2O/Pt(100) interface at 300 K at 0 V vs RHE in alkaline. The full scale is given in Supplementary Fig. 11a. (**b**) Axial distribution function of water perpendicular to the surface along z-axis (ZDF). Blue and red lines denote the H_2O/Pt(100) system with and without Me-N_1C_2, respectively. The black line indicates the acidic condition in presence of Me-N_1C_2. The arrow highlights the H_2O^{2nd} bonded with the $\uparrow H_2O^{1st}$. (**c**) Atomic

configuration of a equilibrated H_2O/Me-N_1C_2/Pt(100) interface at 300 K in alkaline. The full scale is given in Supplementary Fig. 11b. (**d**) Schematic illustration of an interfacial water dimer composed of an $\downarrow H_2O^{1st}$ and $\downarrow H_2O^{2nd}$ bonded with the N_3 of Me-N_1C_2. The numbers and letters represent the height of atoms from Pt surface and the atomic distances, respectively. The corresponding water dimer in (a) and (c) is represented by spheres. The time evolution of the bond distances during the Volmer step at the H_2O/Pt(100) interface (**e**) with and (**f**) without Me-N_1C_2 in alkaline. The grey, brown, blue, red, and white spheres in (a) and (c) represent Pt, C, N, O, and H atoms, respectively.

We then carried out metadynamics simulations[36] to examine how the Me-N_1C_2 affects the Volmer step ($H_2O + e^- \rightarrow H_{ad} + OH^-$) that has been acknowledged as the rate-determining step (rds) of the HER of Pt in alkaline.[3,19] In the absence of Me-N_1C_2, as a biased potential is applied, the Vomer step occurs around 920 femtosecond (fs) as indicated by the significant elongation of the O-H bond (a in Fig. 4d) in the $\downarrow H_2O^{1st}$ (Fig. 4e). This step is triggered by the specific adsorption of the $\downarrow H_2O^{1st}$ ($\downarrow H_2O_{ad}$) as reflected by the abrupt shortening of the Pt-H bond distance to ~1.5 Å. Upon the $\downarrow H_2O_{ad}$ dissociation, the $\downarrow H_2O_{ad}$-Pt bond shortens from 2.74 Å to 1.91 Å, which indicates that the generated hydroxide moves towards the Pt surface and becomes chemisorbed (OH_{ad}). The atomic trajectory of this process is provided in Supplementary Video 1. Its kinetic barrier is estimated as 0.82 eV (detailed calculations given in Methods).

With the presence of Me-N_1C_2, once a hydroxide is generated from the $\downarrow H_2O_{ad}$ dissociation at around 650 fs, the $\downarrow H_2O^{2nd}$ bonded with the Me-N_1C_2 immediately transfers its proton to the hydroxide before it adsorbs to the surface, thereby replenishing the $\downarrow H_2O^{1st}$ (b in Fig. 4f). Then, the OH^- diffuses into bulk solution through the Grotthuss mechanism with about 50 fs for each proton hopping[37,38] (Supplementary Video 2), in contrast to the case absent of Me-N_1C_2. The barrier of this process is calculated as 0.28 eV, much lower than that without Me-N_1C_2. These results indicate that Me-N_1C_2 greatly lowers the energy barrier of the Vomer step of Pt in alkaline and facilitates the diffusion of OH^- across the interface via the Grotthuss

mechanism. Experimentally, we found adding 10^{-5} M N-methylimidazoles into 0.1 M KOH substantially delays the CO oxidation on Pt/C (Supplementary Fig. 12). This observation indicates that N-methylimidazoles impede specific adsorption of hydroxides, in line with our metadynamics simulations.

The key difference between the Volmer steps with and without Me-N_1C_2 is that the $\downarrow H_2O^{2nd}$ bonded with the Me-N_1C_2 donates a proton to the $\downarrow H_2O_{ad}$ whereas the $\downarrow H_2O^{2nd}$ in pure water does not. We postulate this difference is ascribable to Me-N_1C_2 holding the $\downarrow H_2O^{2nd}$ much closer to the Pt surface (3.68 Å) via the $N_3\cdots H_2O$ bonding than the $\downarrow H_2O^{1st}$ via the H-bond (4.34 Å). This can be rationalized by the N_3 being much closer to the Pt surface (2.08 Å) than the O of the $\downarrow H_2O^{1st}$ (3.14 Å). The lowering of the $\downarrow H_2O^{2nd}$ persists during the Volmer step (Fig 4e and 4f), which facilitates the OH^- diffusion through it, thereby promoting the HER/HOR of Pt. The strong $N_3\cdots H_2O$ bonding holds the $\downarrow H_2O^{2nd}$ close to Pt surfaces, which we speculate is indirectly affected by -CH_3(s) via modulating the charge of the N_3 and orientation of the imidazole ring.

Discussions: The HER/HOR processes on Pt. While only the $\downarrow H_2O$ is present in the first water layer on the Pt(100) surface in alkaline condition, both $\uparrow H_2O^{1st}$ and $\downarrow H_2O^{1st}$ are present on the Pt(100) surface in acid (Supplementary Fig. 13). According to the calculated vibrational density of states (vDOS) of the water molecules using the 2PT analysis,[39] the $\uparrow H_2O^{1st}$ has shorter wavenumbers for O-H stretching than the $\downarrow H_2O^{1st}$ (Supplementary Fig. 14), in consist with experimental data.[22,23] These results, in combination with the blue-shift of the ATR-SEIRAS spectra with reducing potentials observed in the 0.1 M KOH free of Me-N_1C_2 (Fig. 3a), support the reorientation from $\uparrow H_2O^{1st}$ to $\downarrow H_2O^{1st}$ with the increasing interfacial electric field (IEF). The O-H stretching wavenumber of the $\downarrow H_2O^{2nd}$ bonded with Me-N_1C_2 are lower than those of the $\downarrow H_2O^{2nd}$ and comparable to those of the $\uparrow H_2O^{1st}$ (Supplementary Fig. 14). This result suggests

that the absence of the shift in the ATR-SEIRAS spectra with potential observed with Me-N_1C_2 in solution (Fig. 3b) can be ascribed to the strong $N_3\cdots H_2O$ bonding.

The average $\uparrow H_2O^{1st}$-Pt distance is 2.21 Å, much shorter than the $\downarrow H_2O^{1st}$-Pt distance (3.14 Å) (Fig. 4b) but comparable to the Pt-N_3 bond distance (2.08 Å). Consequently, the $\downarrow H_2O^{2nd}$ forming H-bonding with this $\uparrow H_2O^{1st}$ has an average $\downarrow H_2O^{2nd}$-Pt distance of 3.54 Å, much shorter than that of the $\downarrow H_2O^{2nd}$ without Me-N_1C_2 (4.34 Å) in alkaline condition but comparable to that (3.68 Å) of the $\downarrow H_2O^{2nd}$ bonded with Me-N_1C_2 (Fig. 4b). The $\uparrow H_2O^{1st}$ holding the $\downarrow H_2O^{2nd}$ close to the surface is a classic bilayer structure model (Fig. 5a) proposed for the electrified Pt-water interface.[22,40] We infer that this $\downarrow H_2O^{2nd}$ can donate its H to the $\uparrow H_2O^{1st}$ during the Volmer step, like the $\downarrow H_2O^{2nd}$ bonded with Me-N_1C_2.

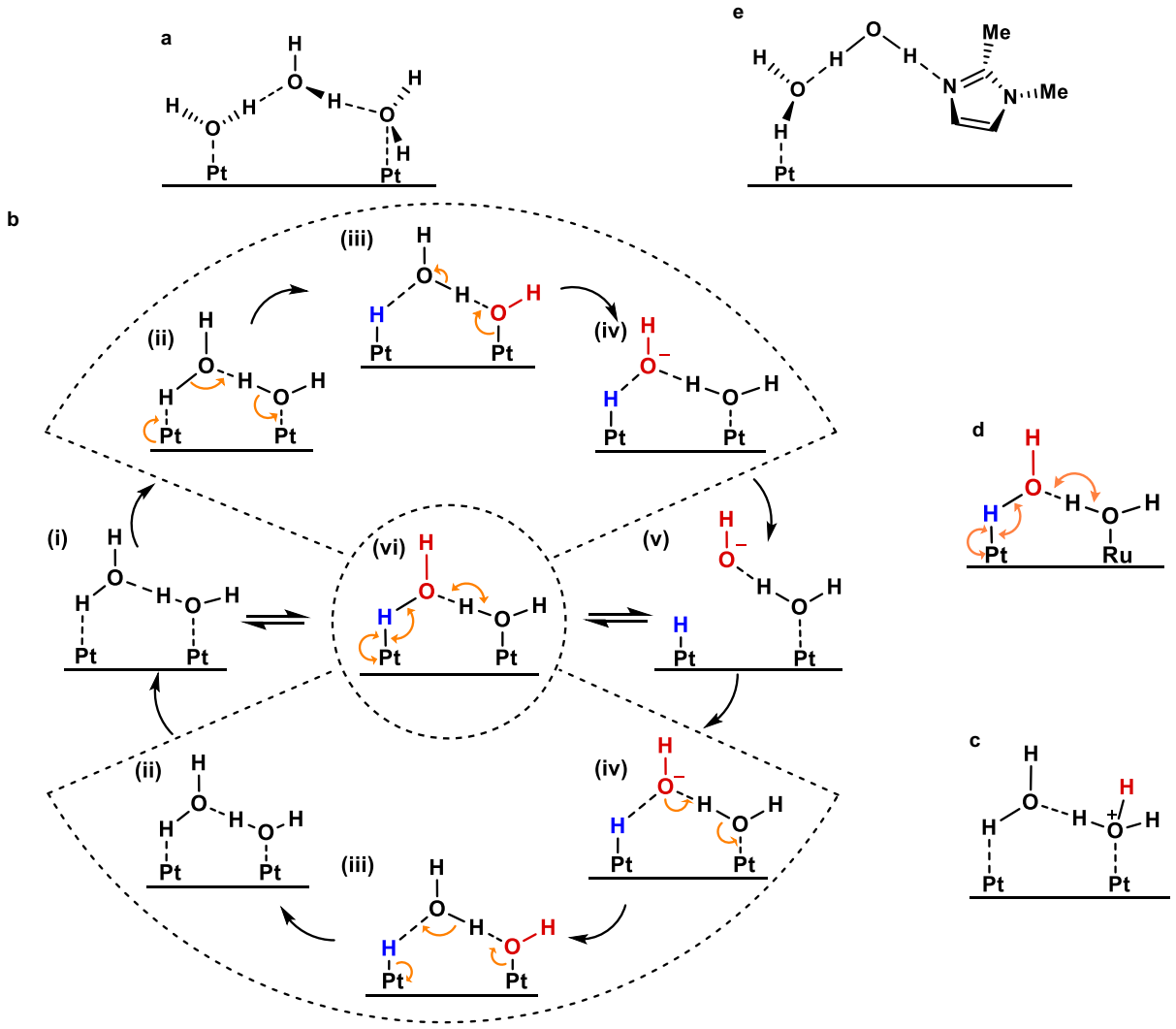

Fig. 5: **Proposed mechanisms for the Volmer process on Pt surfaces**. (**a**) Schematic drawing of a classic bilayer structure of water at the Pt surface, deduced from AIMD calculations. (**b**) The elementary steps of the Volmer process of Pt surfaces in base, by which the water molecule specifically adsorbs onto Pt surfaces, triggering PCET to donate a proton to the Pt surface coupled with an electron donation from the Pt surface, which is accompanied by the transfer of a proton from neighboring water, leading to the formation of an $\uparrow H_2O_{qad}$ (in the dashed circle) through a H_{ad} (blue) and a hydroxide (red) above. (**c**) Schematic drawing of a classic bilayer structure of water at the interface between the acidic solution and Pt surface. (**d**) surface Ru stabilizes $\uparrow H_2O^{1st}$; and (**e**) Me-N_1C_2 stabilizes the $\uparrow H_2O^{2nd}$ on the Pt surface. The orange arrows represent the direction of electron transfer. Solid and dashed lines represent the covalent and non-covalent bonds, respectively, as defined in Ref[41]. The different number of dashes indicates different bond lengths. Here a solid wedge indicates this bond or group is projecting out towards the viewer; a broken (hashed) wedge indicates this bond or group is receding away from the viewer. The ring in (e) is therefore parallel to the Pt surface.

An alternative bilayer structure model is that the $\uparrow H_2O^{1st}$ binding with the $\downarrow H_2O^{1st}$ (Fig. 5b).[40] The Volmer step based on this model in alkaline (Fig. 5b, (i) → (iii)) was recently formulated by Hammes-Schiffer group[42]. By the formulation, the $\uparrow H_2O_{ad}$ donates its H to the $\downarrow H_2O_{ad}$ after its dissociation. This step is coupled with circulation of an electron from the Pt surface to the $\downarrow H_2O_{ad}$, $\uparrow H_2O_{ad}$, and then back to the Pt surface as indicated by yellow arrows in Fig. 5b, (ii)[42,43]. This OH_{ad} naturally forms an H-bond with the newly formed H_2O molecule above (Fig. 5b (iii)) and can therefore diffuse into the bulk electrolyte through it (Fig. 5b, (iii) → (iv). The reverse direction (Fig. 5b, (v) → (i)) describes the Volmer step of the HOR of Pt in alkaline. The net result of the two consecutive processes (Fig. 5b, (ii) ↔ (iv)) are equivalent to the dissociation/formation of the $\downarrow H_2O_{ad}$ via the proton-coupled electron transfer (PCET) process (Fig. 5b, (vi)), which leads to an apparent pathway of (i) ↔ (vi) ↔ (v) without explicitly involving OH_{ad}, as proposed by the Tang groups[44,45].

In both models the $\uparrow H_2O^{1st}$ catalyzes diffusion of OH^- thereby promoting the Volmer step of Pt in alkaline. Likewise, it catalyzes diffusion of H^+ by the Grotthuss mechanism (Fig. 5c).[37] We therefore infer that it facilitates the Volmer step of Pt in acid ($H_{ad} \leftrightarrow H^+ + e^-$) that is governed by diffusion of H^+ across the interface. As pH increases, the $\uparrow H_2O^{1st}$ gets progressively destabilized and/or depopulated by the increasing repelling IEF, and the HER/HOR kinetics of Pt slows down. The diffusion rate of hydroxides in water is about half of that of protons,[46] which may make minor contributions to the two orders of magnitude lower HER/HOR rates of Pt in alkaline than in acid.[3] The major contribution comes from the pH-dependent interfacial water reorientation that governs the H^+/OH^- diffusion.[37,38,46] By this argument, the sluggish HER/HOR of Pt in alkaline can be promoted by surface Ru by stabilizing $\uparrow H_2O^{1st}$ (Fig. 5d) as we proposed

before[17], or by N-methylimidazoles that hold the ↓H_2O^{2nd} close to Pt surfaces like the ↑H_2O^{1st} (Fig. 5e).

Practical application. Reconstruction of interfacial ↑H_2O also promotes HER/HOR kinetics of Pt in practical devices with alkaline media such as anion exchange membrane electrolyzers (AEMELs), for which the repelling interfacial IEF is expected from the high pH environment. By adding 10^{-5} M Me-N_1C_2 into the 0.1 M KOH solution fed into the Pt/C cathode of an AEMEL (See Methods for details), the *i*R-corrected current density at 1.6 V increased by ~40% (Fig. 6). This result demonstrates an alternative route to improve AEMEL performance by introducing organic compounds into the interface.

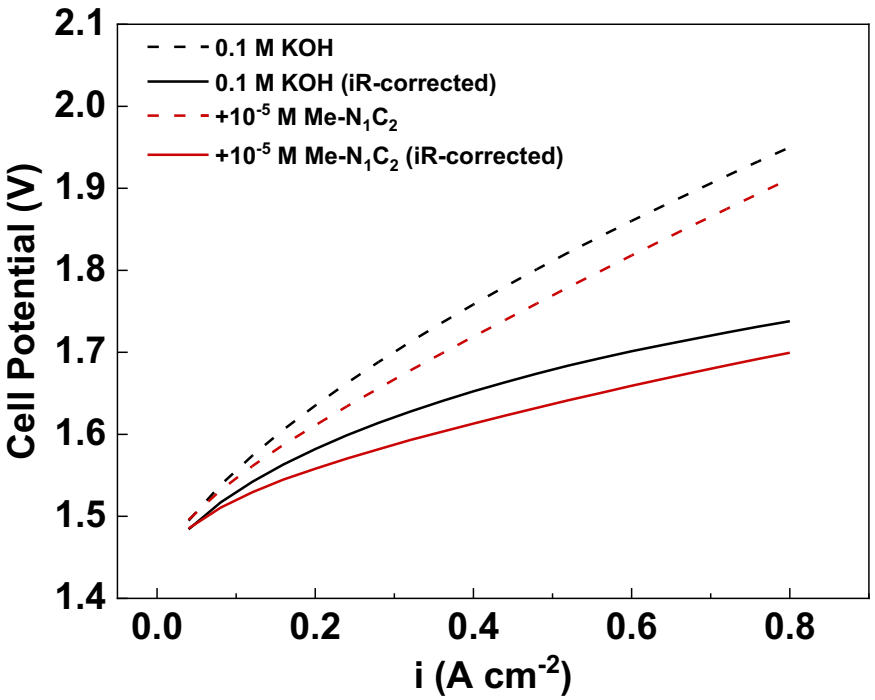

Fig. 6: Me-N_1C_2 improves the AEMEL performance. AEMEL polarization curves with and without adding 10^{-5} M Me-N_1C_2 into the 0.1 M KOH solution fed into the cathode with and without *i*R-correction. Cathode: 0.12 $mg_{Pt}\cdot cm^{-2}$ Pt/C; anode: 3.1 $mg_{IrOx}\cdot cm^{-2}$ IrO_x; membrane: PAP-TP-85-MQN-10C; 60 °C; electrode area 25 cm^2. The resistance with and without adding 10^{-5} M Me-N_1C_2 are 9.5 mohm and 9.7 mohm, respectively.

The Grotthuss mechanism governs proton and hydroxide diffusion through the H-bond network in bulk water. Here we showed that proton and hydroxide diffuse across the Pt-water interface through the H-bond network during the HER/HOR. The interfacial electric field at the electrified Pt/water interface perturbs the interfacial H-bond network by reorientating interfacial water, thereby hindering the diffusion of protons and hydroxides across the interface and in turn the HER/HOR. Restoring the interfacial H-bond network resumes the HER/HOR kinetics**.**

References

1. Sheng, W. *et al.* Correlating hydrogen oxidation and evolution activity on platinum at different pH with measured hydrogen binding energy. *Nat. Commun.* **6** (2015).
2. Zheng, J., Sheng, W., Zhuang, Z., Xu, B. & Yan, Y. Universal dependence of hydrogen oxidation and evolution reaction activity of platinum-group metals on pH and hydrogen binding energy. *Science Advances* **2**, e1501602 (2016).
3. Durst, J. *et al.* New insights into the electrochemical hydrogen oxidation and evolution reaction mechanism. *Energy Environ. Sci.* **7**, 2255-2260 (2014).
4. McCrum, I. T. & Koper, M. T. M. The role of adsorbed hydroxide in hydrogen evolution reaction kinetics on modified platinum. *Nature Energy* **5**, 891-899 (2020).
5. Liu, E. *et al.* Unifying the Hydrogen evolution and oxidation reactions kinetics in base by identifying the catalytic roles of hydroxyl-water-cation adducts. *J. Am. Chem. Soc.* **141**, 3232-3239 (2019).
6. Li, J. *et al.* Experimental poof of the bifunctional mechanism for the hydrogen oxidation in alkaline media. *Angew. Chem. Int. Ed.* **56**, 15594-15598 (2017).
7. Strmcnik, D. *et al.* Improving the hydrogen oxidation reaction rate by promotion of hydroxyl adsorption. *Nat. Chem.* **5**, 300-306 (2013).

8. Schwämmlein, J. N. *et al.* Origin of superior HOR/HER activity of bimetallic Pt-Ru catalysts in alkaline media identified via Ru@Pt core-shell nanoparticles. *J. Electrochem. Soc.* **165**, H229-H239 (2018).

9. Wang, Y. *et al.* Pt–Ru catalyzed hydrogen oxidation in alkaline media: Oxophilic effect or electronic effect? *Energy Environ. Sci.* **8**, 177-181 (2015).

10. Lu, S. & Zhuang, Z. Investigating the influences of the adsorbed species on catalytic activity for hydrogen oxidation reaction in alkaline electrolyte. *J. Am. Chem. Soc.* **139**, 5156-5163 (2017).

11. Elbert, K. *et al.* Elucidating hydrogen oxidation/evolution kinetics in base and acid by enhanced activities at the optimized Pt shell thickness on the Ru core. *ACS Catal.* **5**, 6764-6772 (2015).

12. Ledezma-Yanez, I. *et al.* Interfacial water reorganization as a pH-dependent descriptor of the hydrogen evolution rate on platinum electrodes. *Nature Energy* **2**, 17031 (2017).

13. Intikhab, S. *et al.* Exploiting dynamic water structure and structural sensitivity for nanoscale electrocatalyst design. *Nano Energy* **64**, 103963 (2019).

14. Briega-Martos, V., Ferre-Vilaplana, A., Herrero, E. & Feliu, J. M. Why the activity of the hydrogen oxidation reaction on platinum decreases as pH increases. *Electrochim. Acta* **354**, 136620 (2020).

15. Rebollar, L. *et al.* "Beyond adsorption" descriptors in hydrogen electrocatalysis. *ACS Catal.* **10**, 14747-14762 (2020).

16. Rebollar, L. *et al.* On the relationship between potential of zero charge and solvent dynamics in the reversible hydrogen electrode. *J. Catal.* **398**, 161-170 (2021).

17. Liu, E. *et al.* Interfacial water shuffling the intermediates of hydrogen oxidation and evolution reactions in aqueous media. *Energy Environ. Sci.* **13**, 3064-3074 (2020).

18. Intikhab, S. *et al.* Caffeinated interfaces enhance alkaline hydrogen electrocatalysis. *ACS Catal.* **10**, 6798-6802 (2020).

19. Sheng, W., Gasteiger, H. A. & Shao-Horn, Y. Hydrogen oxidation and evolution reaction kinetics on platinum: acid vs alkaline electrolytes. *J. Electrochem. Soc.* **157**, B1529-B1536 (2010).

20. Alei, M. & Wageman, W. E. ^{15}N NMR shifts for imidazole and 1-methyl imidazole in CH_2Cl_2 relative to aqueous solution. *Tetrahedron Lett.* **20**, 667-670 (1979).

21. Zischang, J., Lee, J. J. & Suhm, M. A. Communication: Where does the first water molecule go in imidazole? *J. Chem. Phys.* **135**, 061102 (2011).

22. Osawa, M., Tsushima, M., Mogami, H., Samjeské, G. & Yamakata, A. Structure of water at the electrified platinum−water interface: a study by surface-enhanced infrared absorption spectroscopy. *J. Phys. Chem. C* **112**, 4248-4256 (2008).

23. Ataka, K.-i., Yotsuyanagi, T. & Osawa, M. Potential-dependent reorientation of water molecules at an electrode/electrolyte interface studied by surface-enhanced infrared absorption spectroscopy. *J. Phys. Chem.* **100**, 10664-10672 (1996).

24. Yao, Y., Zhu, S., Wang, H., Li, H. & Shao, M. A spectroscopic study on the nitrogen electrochemical reduction reaction on gold and platinum surfaces. *J. Am. Chem. Soc.* **140**, 1496-1501 (2018).

25. Li, C.-Y. *et al.* In situ probing electrified interfacial water structures at atomically flat surfaces. *Nat. Mater.* **18**, 697-701 (2019).

26. Toney, M. F. *et al.* Voltage-dependent ordering of water molecules at an electrode–electrolyte interface. *Nature* **368**, 444-446 (1994).

27. Nagy, G. & Heinzinger, K. A molecular dynamics study of water monolayers on charged platinum walls. *J. Electroanal. Chem.* **327**, 25-30 (1992).

28. Wang, S.-H. & Griffiths, P. R. Resolution enhancement of diffuse reflectance i.r. spectra of coals by Fourier self-deconvolution: 1. C-H stretching and bending modes. *Fuel* **64**, 229-236 (1985).

29. Lambert, D. K. Vibrational stark effect of adsorbates at electrochemical interfaces. *Electrochim. Acta* **41**, 623-630 (1996).

30. Teliska, M., O'Grady, W. E. & Ramaker, D. E. Determination of H adsorption sites on Pt/C electrodes in $HClO_4$ from Pt L_{23} X-ray absorption spectroscopy. *J. Phys. Chem. B* **108**, 2333-2344 (2004).

31. Roth, C. *et al.* Determination of O[H] and CO coverage and adsorption sites on PtRu electrodes in an operating PEM fuel cell. *J. Am. Chem. Soc.* **127**, 14607-14615 (2005).

32. Maniguet, S., Mathew, R. J. & Russell, A. E. EXAFS of carbon monoxide oxidation on supported Pt fuel cell electrocatalysts. *J. Phys. Chem. B* **104**, 1998-2004 (2000).

33. Carter, D. A., Pemberton, J. E. & Woelfel, K. J. Orientation of 1- and 2-methylimidazole on silver electrodes determined with surface-enhanced raman scattering. *J. Phys. Chem. B* **102**, 9870-9880 (1998).

34. Papoian, G., Nørskov, J. K. & Hoffmann, R. A Comparative Theoretical study of the hydrogen, methyl, and ethyl chemisorption on the Pt(111) Surface. *J. Am. Chem. Soc.* **122**, 4129-4144 (2000).

35. Cheng, T., Wang, L., Merinov, B. V. & Goddard, W. A. Explanation of dramatic pH-dependence of hydrogen binding on noble metal electrode: greatly weakened water adsorption at high pH. *J. Am. Chem. Soc.* **140**, 7787-7790 (2018).

36. Laio, A. & Parrinello, M. Escaping free-energy minima. *Proc. Natl. Acad. Sci.* **99**, 12562-12566 (2002).

37. Marx, D., Tuckerman, M. E., Hutter, J. & Parrinello, M. The nature of the hydrated excess proton in water. *Nature* **397**, 601-604 (1999).

38. Tuckerman, M. E., Marx, D. & Parrinello, M. The nature and transport mechanism of hydrated hydroxide ions in aqueous solution. *Nature* **417**, 925-929 (2002).

39. Dunnington, B. D. & Schmidt, J. R. Generalization of natural bond orbital analysis to periodic systems: applications to solids and surfaces via plane-wave density functional theory. *J. Chem. Theory Comput.* **8**, 1902-1911 (2012).

40. Ogasawara, H. *et al.* Structure and Bonding of Water on Pt(111). *Phys. Rev. Lett.* **89**, 276102 (2002).

41. Strmcnik, D. *et al.* The role of non-covalent interactions in electrocatalytic fuel-cell reactions on platinum. *Nat. Chem.* **1**, 466 (2009).

42. Lam, Y.-C., Soudackov, A. V., Goldsmith, Z. K. & Hammes-Schiffer, S. Theory of proton discharge on metal electrodes: electronically adiabatic model. *J. Phys. Chem. C* **123**, 12335-12345 (2019).

43. Meng, S., Wang, E. G. & Gao, S. Water adsorption on metal surfaces: a general picture from density functional theory studies. *Phys. Rev. B* **69**, 195404 (2004).

44. Rebollar, L., Intikhab, S., Snyder, J. D. & Tang, M. H. Determining the viability of hydroxide-mediated bifunctional HER/HOR mechanisms through single-crystal voltammetry and microkinetic modeling. *J. Electrochem. Soc.* **165**, J3209-J3221 (2018).
45. Intikhab, S., Snyder, J. D. & Tang, M. H. Adsorbed hydroxide does not participate in the volmer step of alkaline hydrogen electrocatalysis. *ACS Catal.* **7**, 8314-8319 (2017).
46. Chen, M. *et al.* Hydroxide diffuses slower than hydronium in water because its solvated structure inhibits correlated proton transfer. *Nat. Chem.* **10**, 413-419 (2018).

Acknowledgements

This work was supported by the Office of Naval Research (ONR) grant N000141712608 (Q.J.) This research used beamline 7-BM (QAS) of the National Synchrotron Light Source II, a U.S. Department of Energy (DOE) Office of Science User Facility operated for the DOE Office of Science by Brookhaven National Laboratory Contract DE-SC0012704. Beamline operations were supported in part by the Synchrotron Catalysis Consortium Grant DE-SC0012335. W.A.G. acknowledges support by the Liquid Sunlight Alliance, which is supported by the U.S. Department of Energy, Office of Science, Office of Basic Energy Sciences, Fuels from Sunlight Hub under Award Number DE-SC0021266.; This work used the Extreme Science and Engineering Discovery Environment (XSEDE) for AIMD simulation, which is supported by the NSF grant number ACI-1548562. S.K. acknowledges support from the Resnick Sustainability Institute at Caltech.

Corresponding authors

Correspondence to Jingkun Li, William A. Goddard III, Yushan Yan, or Qingying Jia.

Author contributions

Q.J. conceived the project, designed the experiments, and proposed the HER/HOR mechanism. Q.S. conducted the electrochemical experiments and the data analysis in S.M.'s lab partly under his supervision. S.T. and J.G. conducted the NMR experiments and analyzed the data. Q.S. helped to prepare the NMR samples. S.K. and W.A.G. planned the AIMD calculations. N.M. and S.L. performed the DFT calculations and contributed to the writing of the DFT computational results. Y.Y. and N.O. conducted the *in situ* ATR-SEIRAS and data analysis. Y.Y. and N.O. repeated electrochemical RDE experiments. Q.S., L.M., and S.E. conducted the XAS experiments and Q.J. did the data analysis. J.L. conducted the *in situ* surface-enhanced Raman and data analysis. Q.S. and I.K. conducted the AEMEL testing and analyzed the data. Q.J. supervised the project and data analysis. Q.J., Y.Y., W.A.G., Q.S., N.O. and S.K. wrote the manuscript and prepared the figures.

Methods

Chemicals

Carbon support Platinum (47.7%, TEC10V50E, TANAKA), Iridium black (99.95% (metals basis), Alfa Aesar), Potassium Hydroxide (99.99%, Sigma-Aldrich), Perchloric Acid (70%, Sigma-Aldrich), Isopropanol (ACS grade, Fisher Scientific), Caffeine (99.7%, Alfa Aesar), 1,3-dimethyluracil (99%, Aldrich), Imidazole (99%, Acros Organics), 1-methylimidazole (99%, Acros Organics), 2-methylimidazole (99%, Acros Organics), 4-methylimidazole (98%, Tokyo Chemical Industry CO., LTD), 2,4-dimethylimidazole (97%, Alfa Aesar), 1,2-dimethylimidazole (98%, Tokyo Chemical Industry CO., LTD), Dichloromethane (99.9%, extra dry, Acros

Organics), Deuterium Oxide (99.8% (Isotopic), Acros Organics), Dichloromethane-d2 (99.9% (Isotopic), Alfa Aesar), Argon (5.0, UN1006 Middlesex Gas), Hydrogen (UN1049, Middlesex Gas) were used as received. Ultrapure water (18.2 mΩ cm^{-1}) was prepared by the Ultrapure water (Type I) Aqua Solutions system.

Electrochemistry experiments

1. Electrochemical cell and electrolyte preparation

Electrochemical condition experiments in acid (0.1 M $HClO_4$) were conducted in a glass cell. The electrochemical measurements in alkaline solution (0.1 M KOH) were performed in a poly (fluorinated ethylene propylene) (PTFE) cell. Before each measurement, all glassware and plastic jars were deep cleaned, then rinsed in ultrapure water at least six times.

The electrolyte was prepared with ultrapure water and perchloric acid or potassium hydroxide. The glassy carbon electrode embedded in PTFE was used as the working electrode with a platinum mesh counter electrode and a reversible hydrogen reference electrode (RHE). The platinum mesh was sonicated in ultrapure water at least six times before being used.

2. Electrode preparation

Before drop-casting, the glassy carbon electrode (0.2463 cm^2) embedded in PTFE was polished mechanically with 0.5 mm, 0.3 mm, 0.05 mm alumina powder and then sonicated in ultrapure water and isopropanol at least three times. Each time took five minutes.

Ink was freshly prepared each time with 2.4 mg 47.7% Pt/C, 2.55 mL ultrapure water, 0.51 mL isopropanol and 7.65 μL 5% Nafion®. The ink was sonicated in the ice-water bath for 1 hour before drop-casting. 5.3 μL ink was used each time to drop-cast on the glassy carbon electrode

with a rotation rate of 450 rpm to achieve a Pt loading of 8 μg/cm^2. The electrode was dried in the air for about 30 minutes before use and rinsed with ultrapure water prior to electrochemical conditions.

3. Electrochemical measurements

All potentials reported in this work are referenced to the RHE. Before the rotating disk electrode (RDE) testing in 0.1 M KOH, the electrode was cycled in a stagnant Ar-saturated 0.1 M $HClO_4$ electrolyte with a scan rate of 500 mV s^{-1} within the potential range of 0.05-1.2 V for 100 cycles. The cyclic voltammetry (*CV*) was performed in a stagnant Ar-saturated 0.1 M KOH at room temperature with a potential range of 0.05-1.0 V vs. RHE at a scan rate of 20 mV·s^{-1}. The HER/HOR polarization curves were obtained through the potential cycling between -0.2-0.9 V in an H_2 saturated 0.1 M KOH at room temperature with a rotation rate of 2,500 rpm and a scan rate of 20 mV·s^{-1}. All polarization curves in this work (Fig. 1, Supplementary Fig.1 and Fig.3-4) were normalized by the geometric surface area of the RDE electrode and *iR*-corrected. Experiments were repeated at least three times and the averaged values were reported with standard deviations.

The HOR kinetic current densities, used for the calculation of exchange current densities were calculated using the Koutecky-Levich equation (*Eq.*1) to adjust for mass transport limitations.

$$\frac{1}{i} = \frac{1}{i_d} + \frac{1}{i_k} \qquad \text{(Eq. 1)}$$

where i is the as-measured current density, i_d is the diffusion-limited current density, and i_k is the kinetic current density. The exchange current density (i_0) was calculated based on the Butler-Volmer equation (*Eq.* 2), by multiplying the slope of the lines of the micropolarization regions (η = ± 10 mV). The value of ($\alpha_a + \alpha_b$) is approximately assumed to be 1.

$$i_0(\alpha_a + \alpha_b) = \frac{RTi_\eta}{F\eta} \quad \text{(Eq. 2)}$$

, where α_a and α_b are anodic and cathodic transfer coefficients; *F* is Faraday's constant; *R* is the ideal gas constant, and *T* is temperature.

4. Impedance measurement

Electrochemical impedance spectroscopy (EIS) measurements were measured with frequencies from 10^5 to 0.1 Hz with an amplitude of 10 mV by using Autolab Potentiostat.

5. Electrochemical deposition of N-methylimidazoles

After *CV* and HER/HOR measurements, the N-methylimidazole was added into 0.1 M KOH to reach a concentration of 10^{-5} M. Then, the polarization curve and the *CV* were recorded in an H_2 or Ar-saturated 0.1 M KOH electrolyte, respectively, using the same procedure as described above. Each measurement was conducted at least three times and the averaged values were reported with standard deviations.

6. CO stripping

Two potential cycles between 0.05 and 1 V in an Ar-saturated 0.1 M KOH were applied to the electrode at the scan rate of 20 mV s^{-1} before the adsorption of carbon monoxide by purging 1% CO at a constant potential of 0.05 V for 15 minutes into the electrolyte. Then Ar was purged into the same electrolyte for 25 minutes at the same potential to remove the CO from the electrolyte. Then two potential cycles between 0.05 and 1.0 V at the scan rate of 20 mV·s^{-1} were recorded.

7. Anion exchange membrane electrolyzer (AEMEL) testing

Carbon cloth loaded with carbon and PTFE prepared by Advent Technologies® was used as the GDL for the cathode, and porous titanium plate (Nel) was used as the anode. The electrode area

was 25 cm^2. 11% PAP-TP-85 in ethanol prepared by Yan's group was used as ionomer, and PAP-TP-85-MQN-10C from the same group with a thickness of 20 μm was used as the membrane.

For the preparation of the cathode, the Pt/C catalyst (47.7%, TKK) and PAP-TP-85 solution were sonicated with ultrapure water and isopropanol in an ice-water bath for 2 hours to obtain a well-dispersed catalyst ink. The catalyst ink was then hand-sprayed on the carbon cloth using the spray gun (iwata, HP-CS) to achieve a Pt loading of 0.12 $mg \cdot cm^{-2}$ and ionomer loading of 25% *vs*. catalyst. A low loading of Pt was used in the cathode here to render the HER kinetics as the limiting factor of the AEMEL performance. For the preparation of the anode, IrO_x and PAP-TP-85 solution were sonicated with ultrapure water and isopropanol in an ice-water bath for 2 hours to obtain a well-dispersed catalyst ink. The catalyst ink was then hand-sprayed on the carbon cloth using the spray gun (iwata, HP-CS) to reach an IrO_x loading of 3.1 $mg \cdot cm^{-2}$ and ionomer loading of 10% *vs*. catalyst.

The AEMEL performance was tested using a homemade water electrolysis setup. 2 L 0.1 M KOH was fed into the anode at a flow rate of 250 $mL \cdot min^{-1}$ and cathode at a flow rate of 200 $mL \cdot min^{-1}$, respectively. Hewlett Packard 6651A System DC power supply was used to provide the voltage and current necessary for the water-splitting reaction. Keysight 34461A digit multimeter was used to precisely collect current and voltage for the polarization curve. The activation of the cell was first carried out at 0.1 $A \cdot cm^{-2}$ for 5 mins and 0.2 $A \cdot cm^{-2}$ for 30 mins. The polarization curve was then recorded at 60 °C by stepping the current density from 0.04 to 0.8 $A \cdot cm^{-2}$ with an increment of 0.04 $A \cdot cm^{-2}$, and each current density was held for three minutes, and the data of the last 30 seconds were averaged and used as the reported value. After the measurement, 0.1 M KOH at both anode and cathode were replaced as fresh one, and Me-

N_1C_2 was added into 0.1 M KOH at the cathode to achieve a concentration of 10^{-5} M. The same procedure was then repeated to collect the polarization curve.

EIS measurements were measured with frequencies from 10^5 to 0.1 Hz with an amplitude of 10 mV by using Autolab Potentiostat.

Characterization

1. NMR measurement

All NMR experiments were performed on a Bruker AVANCE II 400MHz NMR spectrometer using a BBFO probe equipped with z-axis gradient. The ^{14}N-spectra of imidazole, Me-N_1, Me-C_2, Me-N_1C_2 and ^{15}N- spectra of imidazole, Me-N_1, Me-C_4 and Me-$C_{2,4}$ in either 0.1 M KOH solution (90%/10% H_2O/D_2O) or 90%/10% CH_2Cl_2/CD_2Cl_2 were recorded with proton decoupling during data acquisition. For the ^{15}N-experiments, a 2mM $Cr(acac)_3$ was added to each sample to reduce the relaxation times. The chemical shift scales were referenced as outlined in the IUPAC Recommendations of 2001(Ref[47]). Specifically, the ^{14}N- and ^{15}N- chemical shifts are reported relative to liquid ammonium using nitromethane in chloroform (10% v/v) and 1 M $^{15}NH_4Cl$ aqueous solution as external reference, respectively.

2. XAS measurement

Preparation of electrode

A Pt/C catalyst (47.7%, TKK) and Nafion® were sonicated with ultrapure water and isopropanol in an ice-water bath for 1 hour to obtain a well-dispersed catalyst ink. The catalyst ink was then hand-sprayed on the carbon paper using the spray gun (iwata, HP-CS) to achieve a Pt loading of 0.2 $mg \cdot cm^{-2}$ with an i/c = 0.4.

Deposition of Me-N_1C_2

The prepared electrode was cut into 1.5×1.5 cm^2 square and conducted an acid condition process with a scan rate of 50 $mV \cdot s^{-1}$ from 0.05-0.95 V for 100 cycles in an Ar-saturated 0.1 M $HClO_4$. After that, *CV* was collected in 0.1 M KOH with a scan rate of 20 $mV \cdot s^{-1}$ from 0.05-0.90 V in an Ar-saturated 0.1 M KOH. Me-N_1C_2 was then added into 0.1 M KOH to reach a concentration of 10^{-5} M. Potential cycling from 0.05 V to 0.90 V was then applied with a scan rate of 50 $mV \cdot s^{-1}$ until the *CV* became stable. Another *CV* was collected to verify the successful deposition of Me-N_1C_2 on the surface of the electrode by using the same procedure as previously described.

Synchrotron-based XAS

XAS data were collected at the Pt L_3-edge, for both Pt/C electrodes with and without Me-N_1C_2 for comparison, in fluorescence mode at beamline 7-BM of the National Synchrotron Light Source II (NSLS-II) at Brookhaven National Laboratory, NY. A full range of XAS (0-15 $Å^{-1}$ in the K space), including both the extended X-ray absorption fine structure (EXAFS) and X-ray absorption near-edge structure (XANES) spectra, were collected. Each measurement was conducted for at least 10 scans that were later averaged to improve the signal-to-noise ratio.

3. *In situ* ATR-SEIRAS

All spectroscopic experiments were performed in a custom spectroelectrochemical cell with the Si crystal reflecting plane mounted on the side. The chemically deposited polycrystalline Pt film on the prism served as the working electrode, with a graphite rod counter. These were separated with a Nafion® membrane to prevent contamination of the Pt surface. An Ag/AgCl (3.0 M KCl, BASi) reference electrode was used for all experiments. Electrolytes were purified through electrolysis by holding an Au working electrode at a constant negative current, allowing for

deposition of metal impurities on the Au electrode. All spectroscopic measurements were collected with 4 cm^{-1} resolution and at least 64 coadded scans using an Agilent Technologies Cary 660 FTIR spectrometer equipped with a liquid nitrogen-cooled MCT detector. Electrochemical measurements were conducted using a Solartron SI 1260/1287 system. Impedance measurements were conducted at the beginning of each experiment, and the internal resistance (typically 40-90 ohms) was actively corrected for throughout all experiments. Spectra are presented in absorbance with positive peaks signifying an increase and negative representing a decrease in interfacial species.

4. *In situ* surface-enhanced Raman

All spectroscopic experiments were performed in a custom spectroelectrochemical cell. The polycrystalline Ag film deposited on the glassy carbon served as the working electrode, with a platinum wire as counter electrode. An Ag/AgCl (saturated KCl) reference electrode was used for all experiments. The working and counter electrodes were separated with a Nafion® membrane to avoid contamination. The 0.1 M KOH electrolytes were purified as depicted in the *in situ* ATR-SEIRAS experiment. All spectroscopic measurements were carried out using a Raman spectrometer (HORIBA, LabRAM HR Evolution) equipped with an Olympus objective lens (LUMFL, 60x, numerical aperture: 1.10). The excitation wavelength was a visible light laser (532 nm). Electrochemical measurements were conducted using an Ivium (CompactStat) electrochemical workstation, and the current was stabilized for about 5 minutes at each potential before the Raman spectra were collected.

Computational details

The DFT calculations were performed using the Gaussian 16 program[48]. The imidazole, Me-N_1, Me-C_2, Me-C_4, Me-C_5, Me-N_1C_2, and Me-$C_{2,4}$, and Me-$C_{2,5}$ were optimized using hybrid density functional PBE0[49]-GD3BJ[50] with the aug-cc-pVTZ[51] basis set with the integral equation formalism variant of the polarizable continuum model[52] (IEF-PCM) with parameters for water. We performed a vibrational analysis to confirm that each stationary point is a minimum (only positive vibrational frequencies). A natural bond orbital (NBO) analysis[53] was performed to provide the atomic partial charges.

For imidazole, Me-C_2, Me-C_4, and Me-$C_{2,4}$, the rapid averaging of N_1 and N_3 charge via proton exchange (that is, the proton is instantaneously shared by N_1 and N_3) that occurs at aqueous solution with pH>10 (Ref[20]) were taken under consideration to determine the charge of N_3. Detailed calculations are given in Supplementary Note 1.

AIMD calculations. To obtain a well equilibrated water structure on Pt surface, we first simulated the water/Pt(100) interface using 60 explicit water molecules on a 4×4 Pt(100) surface slab (3 layers) with an area of 1.23 nm^2 and a height of 40 Å along the z-axis. To equilibrate the waters interacting with the interface, we carried out 2 ns of reactive molecular dynamics simulations with 0.25 fs time step using the reactive force field (ReaxFF) for Pt and 60 H_2O.[54] The ReaxFF molecular dynamics simulation was carried out using Largescale Atomic/Molecular Massively Parallel Simulator (LAMMPS)[55] with user package of Reax/C.[56] NVT simulations were performed with a time step of 0.25 fs, using the Nose-Hoover thermostat[57] at 298 K with a damping parameter of 100 fs.

Starting from the geometry with fully connected hydrogen bond network, we removed 3 H_2O and added a target organic molecule. Then, we carried out ab initio AIMD simulation at 298 K for 30 ps to 70 ps for the system to reach equilibrium. Our AIMD simulations used the Vienna

ab initio simulation package (VASP ver. 5.4.5)[58,59] with the VASPsol solvation model.[60] Electron exchange and correlation were treated within the generalized gradient approximation (GGA)[61] in the form of the PBE functional, including the D3 correction for London Dispersion (van der Waals attraction).[62] The interaction between the ionic core and the valence electrons was described by the projector-augmented wave (PAW) method.[63] We used a plane-wave basis set with an energy cutoff of 400 eV. The convergence criteria for the electronic structure was 10^{-5} eV. Only the top surface Pt was allowed to move, with the sublayers fixed to the bulk lattice parameters. The Brillouin zone was only sampled at gamma point of Brillouin zone without any symmetry. The hydrogen mass of water is set to 2 atomic mass unit (D_2O) for a more accurate description of water in classical dynamics. The Nose-Hoover thermostat was applied to keep the temperature at 298 K using a temperature damping parameter of 100 fs. The velocities were rescaled every 20 steps to readjust the target temperature to equilibrium.

To obtain the kinetic barrier of the Volmer step, a metadynamics simulation was performed using the last atomic configurations and velocities from the equilibration. The collective variable (CV) was defined as the difference between two atomic distances: $CV = d_{Pt-H} - d_{O-H}$, where d_{Pt-H} is the distance between the surface Pt atom and the H atom of the interfacial water, and d_{O-H} is the bond length of the water. This variable induces proton transfer from interfacial water to the Pt surface. The starting structures including the atomic configurations and velocities and predictor-corrector coordinates for the two systems, $60H_2O$/Pt and Me-N_1C_2*/$57H_2O$/Pt (parallel) (Supplementary Fig. 11) are provided as Supplementary Data 1 and 2, respectively. A time-dependent bias potential was applied with 20 fs time intervals with Gaussian height (h) of 0.08 eV and width (w) of 0.18 eV. To prevent the water diffusion from the interface to bulk water without Volmer reaction, a single Gaussian hill with h = 1.0 eV and w

= 0.2 eV is applied to guide the metadynamics not to exceed the CV = 2 Å. After the barrier crossing, the kinetic barrier was then calculated by summing the Gaussian potential. The deposition history of Gaussian potential with and without Me-N_1C_2 are provided in Supplementary Data 3 and 4, respectively. The time evolution of CV and potential energy landscape as a function of CV with and without Me-N_1C_2 (Supplementary Data 5-6) are displayed in Supplementary Fig. 15.

Data availability

The data supporting the findings of this study are available within this Article and its Supplementary Information. Additional data are available from the corresponding authors upon reasonable request. Source data are provided with this paper.

References for Methods

47. Harris, R. K., Becker, E. D., De Menezes, S. M. C., Goodfellow, R. & Granger, P. NMR nomenclature. Nuclear spin properties and conventions for chemical shifts (IUPAC Recommendations 2001). *Pure Appl. Chem.* **73**, 1795-1818 (2001).
48. Gaussian 16 Rev. C.01 (Wallingford, CT, 2016).
49. Adamo, C. & Barone, V. Toward reliable density functional methods without adjustable parameters: The PBE0 model. *J. Chem. Phys.* **110**, 6158-6170 (1999).
50. Grimme, S., Ehrlich, S. & Goerigk, L. Effect of the damping function in dispersion corrected density functional theory. *J. Comput. Chem.* **32**, 1456-1465 (2011).
51. Woon, D. E. & Jr., T. H. D. Gaussian basis sets for use in correlated molecular calculations. V. Core-valence basis sets for boron through neon. *J. Chem. Phys.* **103**, 4572-4585 (1995).

52. Tomasi, J., Mennucci, B. & Cancès, E. The IEF version of the PCM solvation method: an overview of a new method addressed to study molecular solutes at the QM *ab initio* level. *J. Mol. Struct.-THEOCHEM* **464**, 211-226 (1999).

53. Dunnington, B. D. & Schmidt, J. R. Dunnington, B. D. & Schmidt, J. R. Generalization of natural bond orbital analysis to periodic systems: applications to solids and surfaces via plane-wave density functional theory. *J. Chem. Theory Comput.* **8**, 1902-1911 (2012).

54. Shin, Y. K., Gai, L., Raman, S. & van Duin, A. C. T. Development of a ReaxFF reactive force field for the Pt–Ni alloy catalyst. *J. Phys. Chem. A* **120**, 8044-8055 (2016).

55. Plimpton, S. Fast parallel algorithms for short-range molecular dynamics. *J. Comput. Phys.* **117**, 1-19 (1995).

56. Aktulga, H. M., Fogarty, J. C., Pandit, S. A. & Grama, A. Y. Parallel reactive molecular dynamics: numerical methods and algorithmic techniques. *Parallel Comput.* **38**, 245-259 (2012).

57. Shuichi, N. Constant temperature molecular dynamics methods. *Prog. Theor. Phys.* **103**, 1-46 (1991).

58. Kresse, G. & Hafner, J. *Ab initio* molecular-dynamics simulation of the liquid-metal--amorphous-semiconductor transition in germanium. *Phys. Rev. B* **49**, 14251-14269 (1994).

59. Kresse, G. & Furthmüller, J. Efficient iterative schemes for ab initio total-energy calculations using a plane-wave basis set. *Phys. Rev. B* **54**, 11169-11186 (1996).

60. Mathew, K., Sundararaman, R., Letchworth-Weaver, K., Arias, T. A. & Hennig, R. G. Implicit solvation model for density-functional study of nanocrystal surfaces and reaction pathways. *J. Chem. Phys.* **140**, 084106 (2014).

61. Perdew, J. P., Burke, K. & Ernzerhof, M. Generalized gradient approximation made simple. *Phys. Rev. Lett.* **77**, 3865-3868 (1996).

62. Johnson, E. R. & Becke, A. D. A post-hartree-fock model of intermolecular interactions: Inclusion of higher-order corrections. *J. Chem. Phys.* **124**, 174104 (2006).

63. Blöchl, P. E. Projector augmented-wave method. *Phys. Rev. B* **50**, 17953-17979 (1994).

Competing interests. The authors declare no competing interests.

Additional information
Figures. S1 to S15
Tables S1 to S5
Videos S1 to S2
Data S1 to S6
Notes 1-3